Frontogenesis and Frontal Progression of a Trapping-Generated Estuarine Convergence Front and Its Influence on Mixing and Stratification

**Sarah N. Giddings · Derek A. Fong · Stephen G. Monismith · C. Chris Chickadel ·
Kathleen A. Edwards · William J. Plant · Bing Wang · Oliver B. Fringer ·
Alexander R. Horner-Devine · Andrew T. Jessup**

Abstract Estuarine fronts are well known to influence transport of waterborne constituents such as phytoplankton and sediment, yet due to their ephemeral nature, capturing the physical driving mechanisms and their influence on stratification and mixing is difficult. We investigate a repetitive estuarine frontal feature in the Snohomish River Estuary that results from complex bathymetric shoal/channel interactions. In particular, we highlight a trapping mechanism by which mid-density water trapped over intertidal mudflats converges with dense water in the main channel forming a sharp front. The frontal density interface is maintained via convergent transverse circulation driven by the competition of lateral baroclinic and centrifugal forcing. The frontal presence and propagation give rise to spatial and temporal variations in stratification and vertical mixing. Importantly, this front leads to enhanced stratification and suppressed vertical mixing at the end of the large flood tide, in contrast to what is found in many estuarine systems. The observed mechanism fits within the broader context of frontogenesis mechanisms in which varying bathymetry drives lateral convergence and baroclinic forcing. We expect similar trapping-generated fronts may occur in a wide variety of estuaries with shoal/channel morphology and/or braided channels and will similarly influence stratification, mixing, and transport.

Keywords Front · Frontogenesis · Trapping · Convergence front · Lateral circulation

S. N. Giddings (✉)
School of Oceanography, University of Washington,
OCN Box 357940, Seattle, WA 98195-7940, USA
e-mail: sarahgid@uw.edu

D. A. Fong · S. G. Monismith · B. Wang · O. B. Fringer
Department Civil and Environmental Engineering,
Stanford University,
473 Via Ortega St.,
Stanford, CA 94305-4020, USA

C. C. Chickadel · W. J. Plant · A. T. Jessup
Applied Physics Laboratory, University of Washington,
1013 NE 40th St.,
Seattle, WA 98105, USA

K. A. Edwards
Ocean Power Technologies,
1590 Reed Road,
Pennington, NJ 08534, USA

A. R. Horner-Devine
Department Civil and Environmental Engineering,
University of Washington,
201 More Hall, Box 352700, Seattle, WA 98195-2700, USA

Introduction

Fronts are regions where two water masses interact, producing intensified gradients in density, turbidity, and/or velocity among other properties. Fronts are ubiquitous in estuaries, typically occurring on relatively small spatial scales and tidal time scales (Largier 1993; O'Donnell 1993). Estuarine fronts have significant implications for transport and aggregation of pollutants (Brown et al. 1991; Klemas and Polis 1977), sediment (Duck and Wewetzer 2001), phytoplankton (Franks 1992; Le Fevre 1986;

Sharples and Simpson 1993), larvae (Wolanski and Hamner 1988), and higher trophic level organisms (Yoder et al. 1994). Hydrodynamic processes associated with fronts influence transport on both intratidal and subtidal time scales thus influencing parameters such as residence time and playing an important role in the temporal and spatial distribution of these constituents. A clear understanding of these processes is needed to better understand estuarine ecosystems and predict the effects of future changes.

Bathymetric complexities, such as a channel with shoals, braiding, or curvature, often contribute to transverse circulation and lateral density gradients that sometimes act to create and/or maintain fronts. In fact, many estuarine fronts, like the one described in this paper, are associated with geometric and bathymetric complexity and transverse circulation (e.g., separation fronts, mixing fronts, and axial convergence fronts, Farmer et al. 2002; Simpson and Hunter 1974; Nunes and Simpson 1985). Various simplified balances driving transverse circulation have been examined in detail. In an unstratified flow, channel curvature (or rotation) can drive secondary circulation with flow towards the outer bank at the surface and towards the inner bank at depth (Falcon 1984; Kalkwijk and Booij 1986). Stratification can establish lateral baroclinic pressure gradients that can in turn induce transverse circulation that can either enhance (e.g., Geyer 1993) or reduce (e.g., Chant and Wilson 1997) transverse flows. The relative magnitude of centrifugal and lateral baroclinic forcing is often unsteady, inducing temporally and spatially dependent secondary circulation suppression, enhancement, and reversal (e.g., Chant 2002; Lacy and Monismith 2001; Nidzieko et al. 2009). Even without curvature, bathymetric variation can lead to lateral baroclinic forcing and transverse circulation via differential advection (Huzzey and Brubaker 1988; Nunes and Simpson 1985; Simpson and Turrell 1986; Valle-Levinson and Lwiza 1995), tidal phase differences (Li and O'Donnell 1997; Scully and Friedrichs 2007; Valle-Levinson et al. 2000), or trapping (Lacy et al. 2003).

In estuaries, shoal/channel interactions and transverse circulation can contribute to altered horizontal dispersion via trapping (Okubo 1973; Fischer et al. 1979; MacVean and Stacey 2010) and/or via altered cross-sectional mixing times (Dronkers and Zimmerman 1982; Fischer 1972; Smith 1976, 1980, 1996). Additionally, these processes can alter vertical mixing (e.g., Lacy et al. 2003). If transverse circulation, or shoal/channel interactions are such that frontogenesis occurs, an important question arises: do fronts inhibit or enhance mixing? Previous observations suggest that mixing near fronts occurs in bursts and/or in localized regions implying that fronts affect the spatial and temporal variability of mixing. Fronts can be regions of high turbulence due to increased shear (Farmer et al. 1995; Farmer et al. 2002; Gargett and Moum 1995;

MacDonald and Geyer 2004). Yet, mixing across fronts can be suppressed or highly localized (O'Donnell et al. 2008) and they may inhibit estuarine flushing (Brown et al. 1991). In fact, the interaction of shoal/channel exchange, transverse circulation, frontogenesis, and mixing are inherently tied together as demonstrated by Lacy et al. (2003). Nonetheless, the details of these complex interactions between fronts, transverse circulation, and mixing remain largely unknown.

In this paper, we examine an estuarine front induced by shoal/channel interactions. After describing the field site and methods employed in "Methods," we include a detailed description of the front and frontogenesis including the transverse circulation and density gradients associated with it, its temporal progression, influence on vertical mixing, spatial progression, and persistence and repeatability in "Results." We then describe the physical mechanisms for frontogenesis, frontal maintenance, and frontal progression ("Discussion"). In the "Conclusions", we explore how this relatively new trapping mechanism fits within the broader context of bathymetrically driven frontogenesis mechanisms and how it may influence transport processes.

Methods

The front we describe here was observed during the COHerent STructures in Rivers and Estuaries eXperiment (COHSTREX) project, a 5-year, multi-institutional collaboration to determine the extent to which the remotely sensed signatures of coherent structures can be used to initialize and constrain predictive models for river and estuarine flows. Overall, this program incorporated a variety of approaches: in situ moorings and transects, transects by an autonomous underwater vehicle (AUV), remote imaging with infrared and visual wavelengths, microwave radars, and high-resolution 3D numerical simulations. This suite of approaches enables us to construct a complete picture of how an individual front forms and evolves.

Field Site: Snohomish River Estuary

The Snohomish River Estuary (SRE) is a shallow, macrotidal, strongly stratified estuary which is part of the second largest drainage basin in Puget Sound (Fig. 1). Flanked by intertidal mudflats and tidal marshes to the north and west, the main channel curves 180° around the reinforced coastline of Everett, Washington, delineated on the west by Jetty Island before connecting to Possession Sound. A second, intertidal, connection to Possession Sound occurs over the mudflats north of Jetty Island hereafter referred to as the mudflat bypass (Fig. 1c).
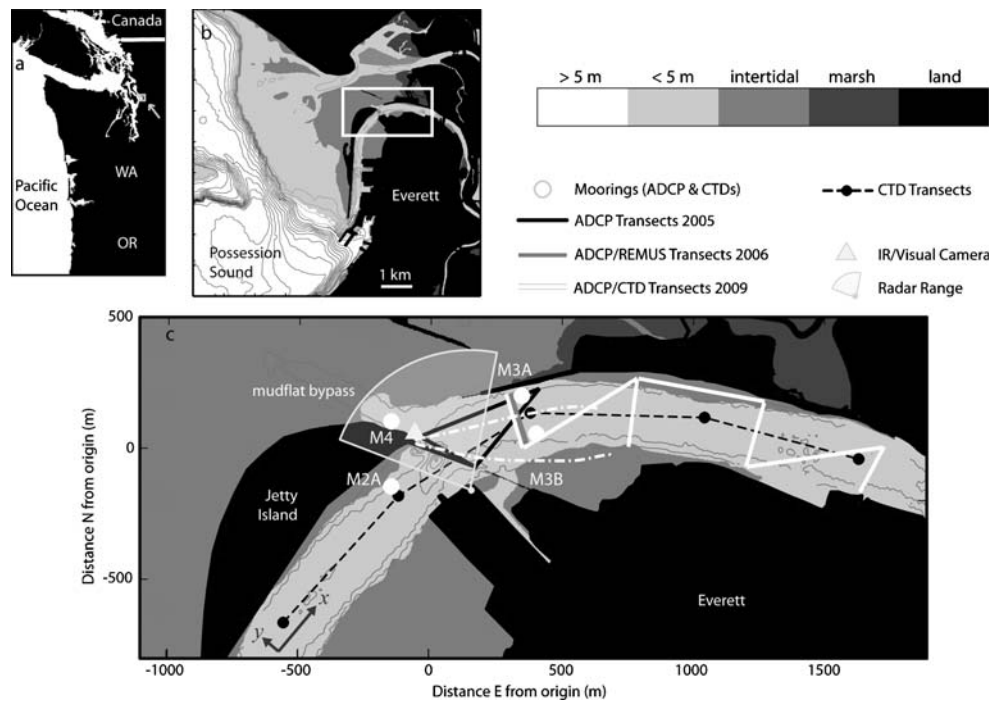
Fig. 1 SRE with instrumentation **a**, **b** SRE, Everett, Washington, Pacific Northwest US coast. Depth contours are every 2 m shallower than 10 m (*lighter gray*) and every 10 m beyond (*darker gray*). Marshes are *dark gray*; intertidal regions are *intermediate gray*; and the *lightest gray* indicates depths less than 5 m below MLLW. *White* indicates depths greater than 5 m below MLLW. **c** Moorings and transects discussed in this paper. Map is centered at 48.02° N, 122.22° W. Positive along-stream (*x*) and cross-stream (*y*) directions are indicated on the figure. Positive along-stream velocity (*u*) is in the direction of the flood tide while positive cross-stream velocity (*v*) is towards the outer bank. Note that the 2006 ADCP transects were in the same location as the REMUS transects and the furthest downriver Sept 2009 transects. *White dashed-dotted lines* indicate two positions of the front: early in the frontal progression (further north) and later in the frontal progression (further south)

The SRE tidal range varies from 3 m (neap) to almost 4.5 m (spring) driving tidal currents exceeding 1.2 ms^{-1}. The main channel depth is ~2.5 m below mean lower-low water (MLLW) leaving only 1.5–2 m of water in the channel at lower-low water and 6 m at higher-high water. The M_2 semidiurnal and K_1 diurnal tidal constituents dominate water level and there is a pronounced fortnightly cycle and strong diurnal inequality. The complex bathymetry, macrotidal, shallow nature of the estuary, and diurnal inequality are important to the front we describe here.

Data presented in this paper are during typical summertime through early autumn conditions (July through October) with a median river discharge ~100 m^{3}s^{-1}, minimal precipitation, and light diurnal winds which are northwesterly approaching maximum speeds of ~6 ms^{-1} in the evening. Under these conditions, during the strong ebb each tidal cycle, the system is essentially re-set to initial conditions where the channel is entirely fresh, riverine water. On the ensuing large flood tide, the salt-wedge intrudes into the system creating strong vertical and horizontal density gradients. During the weak ebb, straining and advection enhance vertical stratification. Stratification is slightly decreased on the weak flood, only to be enhanced again during the strong ebb tide before the salt-wedge advects out of the estuary. A detailed discussion of the SRE circulation and mixing dynamics can be found in Giddings et al. (2011).

Instrumentation

The bulk of the data presented in this paper is from the COHSTREX experiment conducted 5–26 July 2006 although we also include data from experiments in 2005, 2007, and 2009. A map of the SRE is overlain with instrument locations in Fig. 1c. Note that additional instrumentation not discussed in this paper is left off for clarity, and the location of the 2009 moorings (only used for water level in this paper) were located ~10 km upriver from the 2006 site, near the southern extent of Fig. 1b. The coordinate system we employ is oriented so that the along-stream (*x*) direction is positive in the direction of flooding currents (i.e., upriver), while the cross-stream (*y*) direction is positive towards the outer bank of the large curved section. Tidal elevation with respect to MLLW and depth average along-stream velocity (when available) during the experiments are shown in Fig. 2 with sampling times.
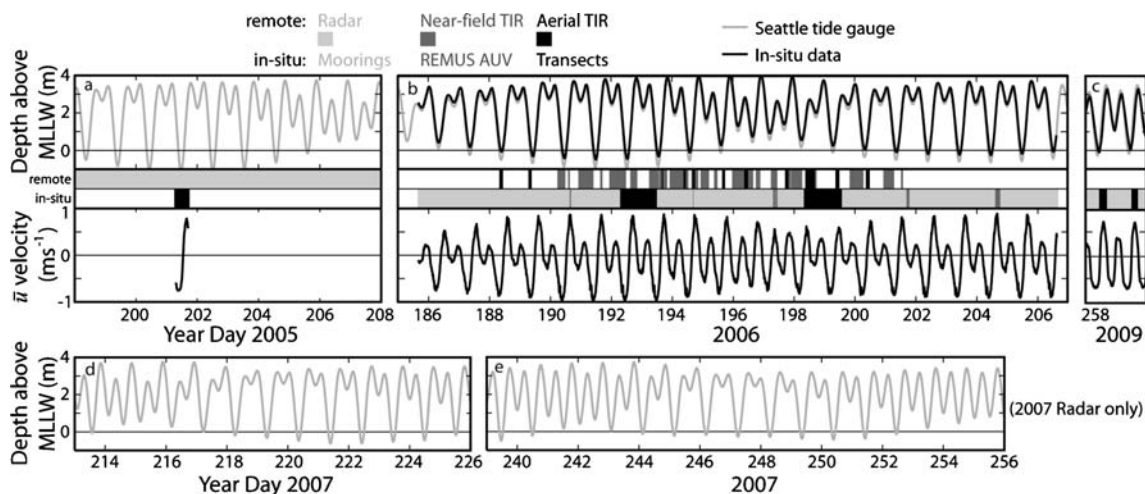
Fig. 2 Water level during sampling periods. Water level during the 2005 (**a**), 2006 (**b**), 2009 (**c**), and 2007 (**d**, **e**) sampling periods are shown with *horizontal bars* indicating the times of different sampling methods. The remote sensing instrumentation shown on the first line includes the RiverRad radar (*light gray*), near-field TIR (*gray*) and aerial TIR (*black*) measurements. The in situ instrumentation shown on the second line includes the moorings (*light gray*), REMUS AUV (*gray*), and boat-mounted ADCP/CTD transect (*black*) measurements. Water level and velocity from moorings are included in *black* when available. No velocity or *horizontal bars* are included on the plots for 2007 as only the radar was operating (continuously) during these time periods

Moored and Boat-Mounted Transecting In Situ Instrumentation

During the July 2006 experiment, a total of six moorings were deployed. For the purpose of this study, we focus on measurements from moorings M3A, M3B, and M4 which provide us with hydrodynamic measurements throughout the frontal region (Fig. 1c). Moorings M3A (outer bank, north) and M3B (inner bank, south) were equipped with bottom-mounted Teledyne RDI Acoustic Doppler Current Profilers (ADCPs) and SeaBird Conductivity Temperature Depth Sensors (CTDs) at multiple depths. The 1,200-kHz ADCPs were operated in mode 12, averaging ten sub-pings per 1-Hz sample with data recorded in beam coordinates in 0.25 m depth bins throughout the water column with the bottom bin centered ~1 m above the bed (mab). The CTDs sampled once per minute. One SeaBird 16+ CTD was mounted on the mooring frame ~0.2 mab while two SeaBird 37s hung beneath a floating buoy (~0.8 and 2 m beneath the water surface) such that they followed the water surface. Mooring M4 had a bottom-mounted Nortek Aquadopp Profiler sampling in 0.4 m bins and a bottom-mounted CTD both sampling once per min.

For transect measurements through the front, a 1,200-kHz RDI ADCP and Seabird SBE19 CTD were mounted to a ~20-ft vessel which was driven at speeds of less than 1.5 ms^{-1}. The ADCP was operated using mode 12 at 1 Hz (ten sub-pings averaged per sample) allowing for ~1 m horizontal resolution. The ADCP recorded velocities in 0.25 m bins starting 1 m beneath the water surface. GPS data were logged concurrently with the ADCP bottom-tracking data to ensure accurate positioning. The CTD was mounted ~0.5 m beneath the water surface, logging at 2 Hz. Thirty-hour transect surveys following a square path around the mudflat confluence were conducted every 20 min during representative spring and neap tides, 12–13 and 18–19 July 2006, respectively. This manuscript focuses on the 3-min transects between moorings M3A and M3B (Fig. 1c, gray line). Additional transects with similar instrumentation were conducted on 21 July 2005 and 16–17 September 2009 following slightly different transect paths (see Fig. 1c). During July 2006, a second boat was used to complete along-stream CTD transects. Casts with a SeaBird SBE19 CTD were taken at five stations along the estuary every half hour (Fig. 1c). The CTD sampled at 2 Hz and was lowered at 10–20 cms^{-1}, resulting in density profiles with 5–10-cm vertical resolution. Cross-channel CTD transects (four casts) were conducted on 23 July 2006 and concurrently with the ADCP transects on 16–17 September 2009.

Autonomous Underwater Vehicle

In July 2006, we used a Remote Environmental Measuring Units 100 (REMUS, Hydroid, Inc.) AUV to make high-resolution cross-frontal measurements. The AUV was equipped with two 1,200-kHz RDI ADCPs (one upward-looking and one downward-looking) and a CTD (4 Hz sampling). The ADCPs averaged four pings and four bottom track pulses at its maximum rate of ~0.5 Hz (~3 m horizontal resolution) in 0.5 m depth bins. Missions from 10 and 24 July involving 90-s transects between M3A and M3B (Fig. 1c, gray line) are utilized in this paper.

Visual and Thermal Infrared Imaging

Visual and thermal infrared (TIR) imaging were conducted from both near- and far-field aerial locations in July 2006 overlooking the frontal region. A long-wave (8–12 μm) AIM model 640Q TIR camera and a visual camera were mounted atop a barge-deployed hydraulic lift ~30 m above the water surface providing a limited field of view (~35× 35 m) with a 5-cm pixel resolution. The periodically calibrated TIR camera has a Noise Equivalent Temperature Difference of <0.05 K. Geo-registered temperature maps, recorded at 2 Hz revealed surface patterns due to frontal convergences as well as surface disruptions and large-scale turbulence (see Chickadel et al. 2009 for more information). An identical temperature-calibrated AIM and visual camera pair were mounted to view at nadir from a Twin Otter airplane providing less temporal resolution but a larger spatial coverage. The plane was nominally flown at an altitude of 610 m, which allowed for thermal imagery with 30-cm per pixel resolution at the water surface and an approximate field of view of 150×200 m.

Radar Imaging

Radar measurements were made 18–26 July 2005, 2–14 Aug 2007, and 27 Aug–14 Sept 2007 using RiverRad, a pulsed Doppler X-band radar built by APL/UW (Plant et al. 2005). RiverRad measures surface currents using the Doppler shifts induced in signals scattered off the rough river surface to two parabolic antennas. It also measures calibrated normalized radar cross sections of backscatter. During these experiments, RiverRad was operated at its highest range resolution of 3.75 m bins over 480 m and was swept through an 80° swath of the river in 20 min (Fig. 1c). For further details on RiverRad operation during this experiment, see Plant et al. (2009). As has been shown in other radar applications to fronts (e.g., Braun et al. 2008; Handler et al. 2001), radar backscatter peaks near the frontal location.

Numerical Process Study

In addition to the instrumentation deployed, the parallel, finite-volume, unstructured-grid SUNTANS solver (developed by Fringer et al. (2006)) was employed to analyze the three-dimensional hydrodynamics of the SRE (Wang et al. 2009). The unstructured grid resolves the large scale, O(10 km) tidal dynamics of the estuary extending to Steamboat Slough, Possession Sound, and Port Susan while allowing fine resolution near the study site, 8 m near the confluence of the main channel and mudflat bypass. The numerical model employs a z-level vertical grid and includes wetting and drying. The model

predictions have been validated for free surface, velocity, and salinity with observations; details are presented in Wang et al. (2009; 2011). The model successfully reproduces frontal formation (Plant et al. 2009) and qualitatively captures the associated circulations and density variations. In this manuscript, the model is used to perform a process study to qualitatively confirm the forces governing the frontal formation and propagation.

Results

Frontal Evolution/Description

The front investigated in this study forms every tidal cycle during peak flood tide as water that was trapped over the mudflat bypass during the previous large ebb tide (mid-density) is pushed back into the main channel (Puget Sound density) when the bypass reconnects to Possession Sound. The convergence of these water masses forms an axial convergence front that stretches from the tip of Jetty Island northeastward along the channel center (see northern most white dashed-dotted line in Fig. 1c). The front is associated with two surface convergent transverse circulation cells accompanied by a visible foam/debris convergence line and sharp density gradient. As the flood tide continues, the front propagates across the channel until it breaks down around slack near higher-high water (southern dashed-dotted white line in Fig. 1c).

The location and surface manifestation of the front as well as its sharp gradients measured by our various instruments on different days near peak flood tide is shown in Fig. 3. The aerial TIR image shows the strong surface temperature signal while the boat- and AUV-mounted CTD measurements show the sharp density discontinuity. Lines marking the frontal location as determined from the radar and numerical simulations tie together these measurements.

A cross section of density anomaly and cross-stream velocity when the front was just south of the channel center near peak flood currents during September 2009 is presented in Fig. 4. The near-surface CTD measurements show the sharp density discontinuity at the front (similar to those seen in Fig. 3); the density difference and local gradient across the front near the surface reached up to 6 kg m^{-3} and $\partial\rho/\partial y \approx 1.6$ kg m^{-4}, respectively. Overlain CTD casts show that the less dense water formed a shallow (~1.5 m) lens resembling a buoyant plume front north of the frontal interface. This led to enhanced vertical stratification where the mudflat water was present (to be discussed in greater detail in "Stratification and Vertical Mixing"). The ADCP measurements show two surface convergent transverse circulation cells coincident with the density interface. Frontal convergence was as high as 0.4 ms^{-1}
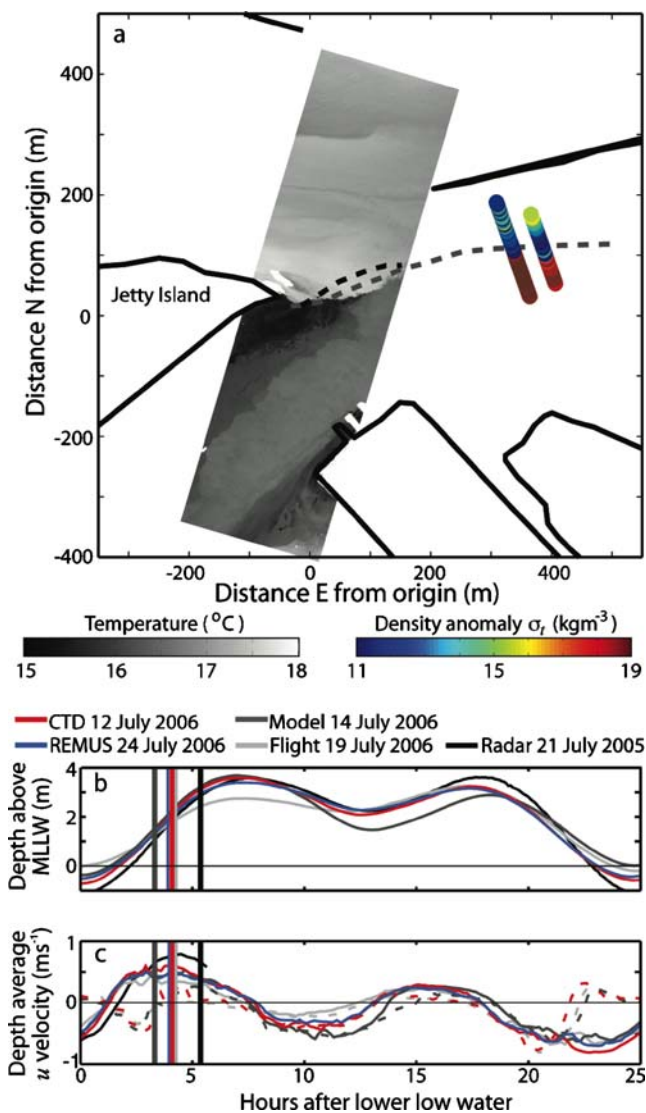
Fig. 3 Frontal images. **a** An aerial TIR image is overlain with the frontal location determined by the RiverRad peak in radar cross section (*black dashed line*) and simulation results (*dashed gray line*) as well as density from the CTD transects and REMUS transects (*color scale dots, offset to right*). **b** Water level and **c** depth averaged along-stream velocity (*u*) measured at mooring M3A (*solid*) and mooring M4 (*dashed*) for each measurement day with the measurement time stamp marked with a *vertical line*

over 20 m, $\partial v/\partial y \approx 0.02 \text{ s}^{-1}$ and usually ranged between 0.01 and 0.02 s^{-1}.

Frontogenesis and Temporal Evolution

The temporal evolution of the along-stream and cross-stream velocities throughout the cross section and near-surface density from the boat-mounted ADCP and CTD transect data along with near-field TIR imagery are shown in Fig. 5 for the spring survey, 12 July 2006. The four rows present data collected during the strong flood tide before (first row), during (middle two rows), and after (last row) of
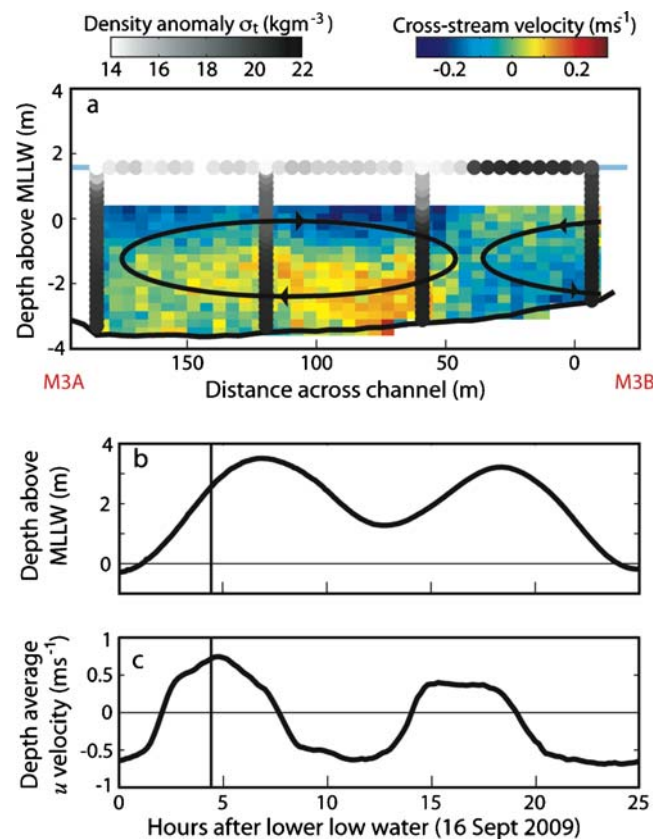

Fig. 4 Frontal cross-stream density distribution. **a** Density anomaly (kg m^{-3}, *gray scale dots*) and velocity (ms^{-1}, *color scale*, positive towards the outer bank, M3A) distribution between moorings M3A and M3B while the front is present on 19 September 2009. Both CTD casts (taken at ~60 m intervals: 15, 80, 140, and 205 m) and concurrent higher spatial resolution near-surface CTD measurements are included. The outer bank (M3A, north) is on the left and the inner bank (M3B, south) is on the right such that one is looking in the flood direction. *Bottom panels* include water level (**b**) and velocity (**c**) during this tidal cycle with a *black vertical line* indicating the time when the transect was conducted

the front. Time series of salinity, temperature, vertical density stratification, water level, and depth averaged along-stream velocity at the moorings (Fig. 6) describe the temporal progression in additional detail. Vertical lines on Fig. 6 (left to right, t_1–t_4) correspond to the same time periods as the four rows in Fig. 5 (top to bottom).

During the previous large ebb, density decreased at all of the moorings as the salt-wedge moved downriver. Around day 192.4, the mudflats were shut off from Possession Sound prohibiting flow out that direction. Salinity in the main channel continued to drop; while over the mudflats it remained at a mid-salinity value suggesting this water mass was trapped over the mudflats (Fig. 6). Upon the start of the large flood, there was a brief input of fresh water from the main channel into the mudflat region consistent with the mudflats still being disconnected from Possession Sound and velocity over the mudflats becoming negative (from the
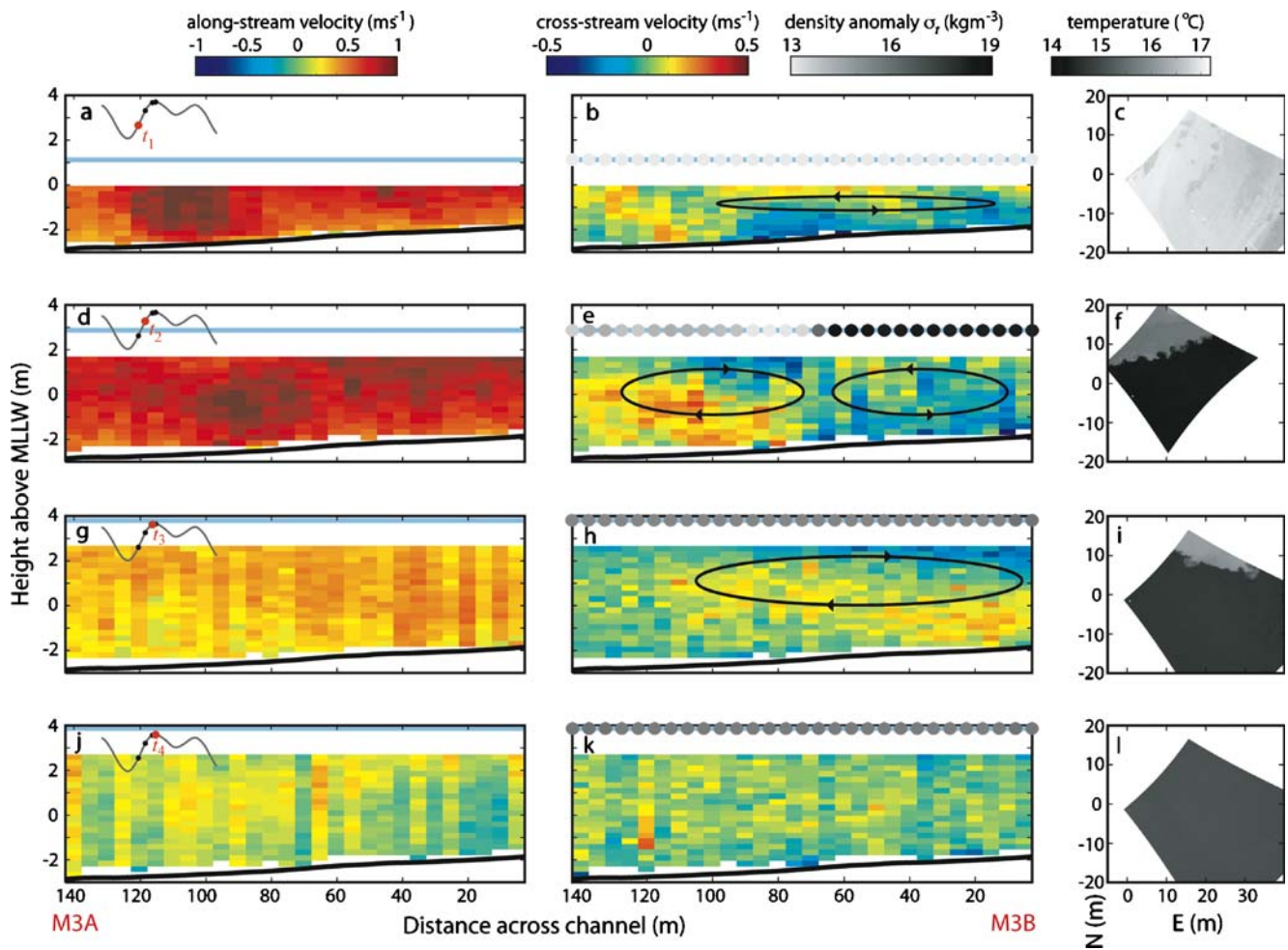
Fig. 5 Temporal frontal evolution. *Left panels* show the along-stream flow (ms⁻¹, positive with flooding currents) and *middle panels* show the cross-stream flow (ms⁻¹, positive towards the outer bank, M3A) throughout the cross section between moorings M3A and M3B measured by the boat-mounted ADCP. *Middle panels* also include *dots* indicating the near-surface density anomaly (kg m⁻³, gray scale) from the boat-mounted CTD. The far right panels show near-field georeferenced TIR images from the same time (°C) referenced in m relative to the origin shown in Fig. 1c. *Each row* represents a point in time during the flood tide from before the front exists (*top panel*), during the front (*middle two panels*), to after the front has dissipated (*bottom panels*). These points in time are marked as *dots* on an inset of the water level on the left panels and as *vertical lines* t_1–t_4 on Fig. 6

main channel to the mudflats) (Fig. 6; t_1=192.65). The main channel exhibited vigorous transverse circulation consistent with curvature-driven circulation, i.e., towards the outer bank at the surface (positive v) and towards the inner bank at depth (negative v) (Fig. 5b).

Shortly after this, the salt-wedge passed upriver as indicated by the rapid increase in main channel density (Fig. 6, just after t_1). Following the salt-wedge passage in the main channel, the mudflat region re-connected to Possession Sound and the mudflat flow reversed becoming positive (from the mudflats towards the main channel; Fig. 6e). During this time, mid-density water stored there was pushed into the main channel and a front formed between these two water masses. Mooring M3A became stratified and the top CTD density matched that of the water coming from the mudflats (Fig. 6, t_2=192.72). The

front was strongest near peak flood currents when it was situated along the channel center near the northern dashed-dotted white line in Fig. 1c (Fig. 5d–f). Strong surface convergent circulation cells were coincident with the sharp density interface (Fig. 5e) and the concurrent TIR image (Fig. 5f) identifies the front with warmer water coming from the mudflats converging with colder water in the main channel.

As the flood weakened, the front propagated across the channel south of M3B (i.e., near the southern dashed-dotted white line in Fig. 1c) such that the outer bank circulation cell had grown to encompass the region between moorings M3A and M3B (Fig. 5g, h) and mudflat water was spread across the top of the channel beyond mooring M3B such that M3B was also vertically stratified with near-surface density similar to mooring M3A (Fig. 6, t_3=192.80). The
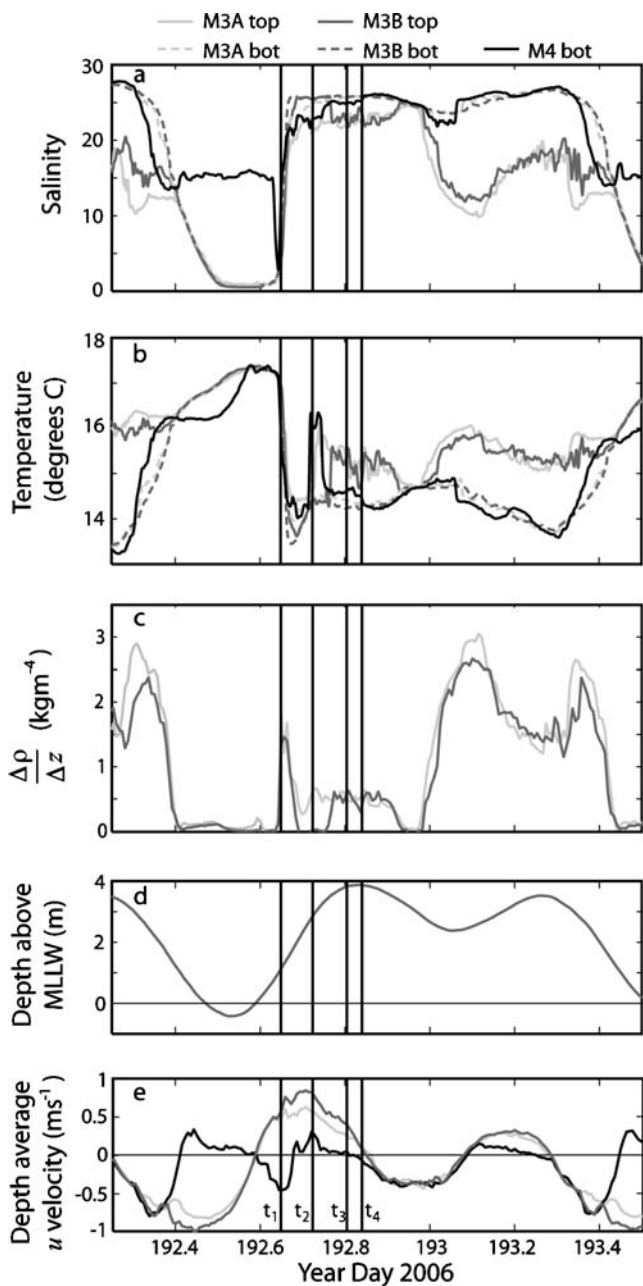
Fig. 6 Temporal evolution of currents, salinity, temperature, and stratification at moorings M3A, M3B, and M4. **a**–**e** Include salinity, temperature (°C), top–bottom vertical density stratification (kg m^{-4}), water level (m), and depth averaged along-stream velocity (ms^{-1}), respectively for moorings M3A (*light gray*), M3B (*gray*), and M4 (*black*). In (**a**) and (**b**), M3A and M3B include near-surface (*solid lines*) and near-bottom (*dashed lines*) measurements. *Vertical lines* correspond to each row in Fig. 5 and are the same time stamps, t_1–t_4 shown in Figs. 8 and 9

ADCP transects did not go far enough towards the inner bank to observe a circulation cell there but due to the consistently observed presence of the convergent foam line well after it passed south of mooring M3B and the TIR confirmation of the frontal presence (Fig. 5i), we speculate

that the inner bank circulation cell was still present, although smaller and potentially weaker.

Finally, as the front pinched off on the other side of the channel and the currents weakened substantially, the front was no longer present and the channel experienced minimal transverse circulation (Fig. 5j–l). Despite the disappearance of the front, the main channel remained stratified from the buoyant mudflat input that had spread across the channel (Fig. 6, t_4=192.84). Figure 7 summarizes the frontal evolution described above.

Stratification and Vertical Mixing

As previously described, the strong density differences associated with the front influence the temporal and spatial variability of stratification in the region which will in turn influence vertical mixing. Throughout the frontal propagation period, the region to the north of the frontal interface is stratified, while the region to the south is vertically well mixed (recall t_2 and t_3 in Figs. 5 and 6). Importantly, even after the front was gone, stratification persisted as the buoyant water formed a thin upper layer across the channel (t_4). This is significant because it is inconsistent with the standard view of strain-induced periodic stratification (SIPS) (Simpson et al. 1990); SIPS suggests flood straining is destabilizing and should lead to minimal stratification at the end of flood tides rather than enhanced stratification as observed here.

The degree of turbulent vertical mixing depends on the competing effects of stratification and shear such that we expect vertical mixing to respond to these temporal and spatial variations in stratification. We assess the influence of the front on vertical mixing with measurements of the gradient Richardson number (Ri_g) and of turbulent kinetic energy production (P) on either side of the front. Ri_g (Turner 2001) was estimated using velocity and density at each mooring:

$$Ri_g = \frac{N^2}{S^2} = \frac{-\frac{g}{\rho_o}\frac{\partial \rho}{\partial z}}{\left(\frac{\partial u}{\partial z}\right)^2 + \left(\frac{\partial v}{\partial z}\right)^2} \cong \frac{-\frac{g}{\rho_o}\frac{\Delta \rho}{\Delta z}}{\left(\frac{\Delta u}{\Delta z}\right)^2 + \left(\frac{\Delta v}{\Delta z}\right)^2} \tag{1}$$

We also directly computed P with ADCP measured Reynolds stresses and shear:

$$P = -\langle u'w' \rangle \frac{\partial u}{\partial z} - \langle v'w' \rangle \frac{\partial v_n}{\partial z}$$

$$\cong -\langle u'w' \rangle \frac{\Delta u}{\Delta z} - \langle v'w' \rangle \frac{\Delta v}{\Delta z} \tag{2}$$

The Reynolds stresses were computed using the variance technique (Lu and Lueck 1999; Nidzieko et al. 2006; Stacey et al. 1999) and the cubic spline smoothing parameter, P=0.99, was chosen such that the error in the
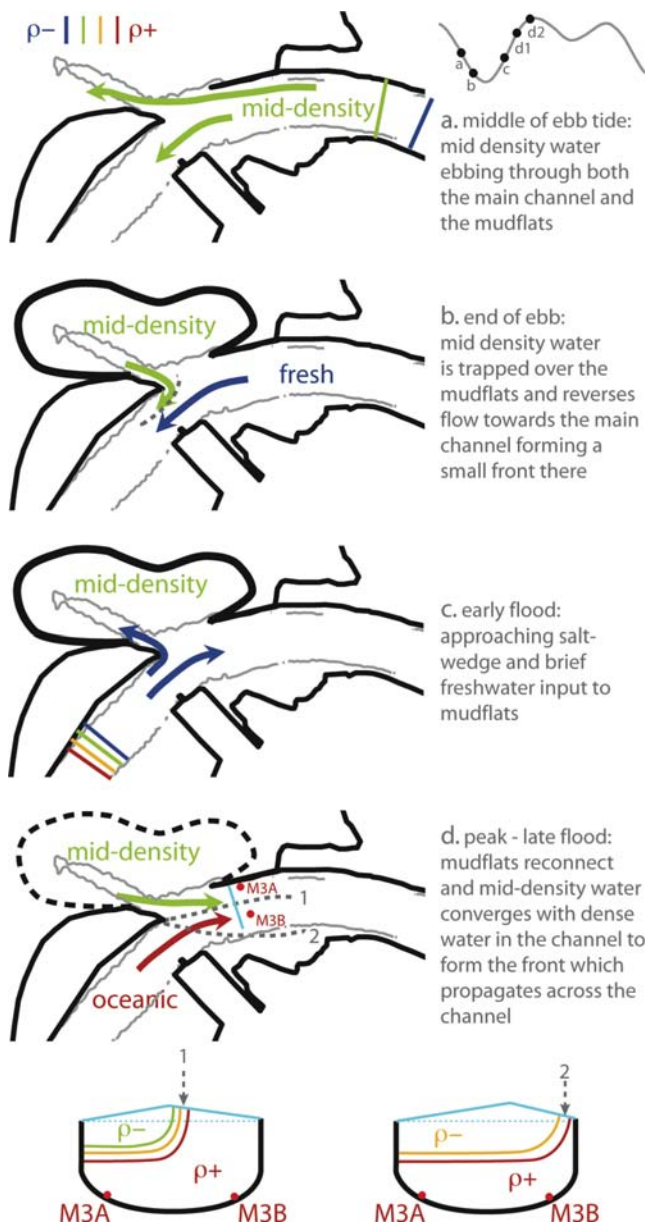
Fig. 7 Sketch of frontogenesis trapping mechanism. **a–d** Step through mid-ebb through late flood tide sketching the frontal formation via the trapping mechanism. A *solid thick line* around the mudflats represents no exchange with Possession Sound from that direction; a *dashed line* indicates hydrodynamic connectivity between the mudflats and the sound while *no line* indicates full exchange between the mudflats and the sound, i.e., fully submerged mudflats. The bottom of (**d**) includes cross sections between moorings M3A and M3B to demonstrate the density distribution and potential water surface setup (exaggerated) soon after the front forms near peak flood (d1, similar to time t_2 in other figures) and just before the front breaks down (d2, similar to time t_3 in other figures)

difference between the raw and smoothed stresses was similar to the error in the stress measurements.

Ri_g and P are plotted in Fig. 8 for the same time periods displayed in Figs. 5 and 6 for moorings M3A (left panels) and M3B (right panels). The variation of Ri_g and P over the

tidal cycle and the fortnightly cycle are discussed in Giddings et al. (2011). Here we focus on the measurements during the large flood tide as the front evolves focusing on the same four times discussed previously. Prior to frontal formation (t_1) the system was briefly stratified and mixing was suppressed across the entire channel as indicated by a high Ri_g and low P at both moorings as the sharp salt-wedge passed upriver. After the salt-wedge passed upriver and the front formed and moved towards the channel center, different mixing was observed on either side of the channel (t_2). Active turbulent vertical mixing at M3A was limited to a small bottom boundary layer capped by a region of inhibited mixing due to stratification induced by the overlying lower density mudflat water. High Ri_g and low P throughout the water column except near the bed indicate this. In contrast, mooring M3B experienced strong bottom-generated P that extended higher into the water column. The very low Ri_g and high P indicates the potential for mixing throughout the water column at M3B. This strong bottom-generated P was suppressed when the front moved further across the channel, south of mooring M3B, when overlying lower density water stratified this side of the channel as well (t_3). At this time, both moorings exhibited high Ri_g throughout the water column indicating that the effects of stratification exceeded shear. These conditions of inhibited vertical mixing persisted after the front dissipated due to the persistence of the front-induced stratification and minimal P (t_4).

Spatial Evolution

The measurements presented thus far were near the mudflats where the front is generated; however the front also evolves spatially upriver. Transects collected in September 2009 further upriver do not display the same strong frontal features. Upriver, transverse circulation was consistent with curvature (i.e., towards the outer bank at the surface and the inner bank at depth) and exhibited more gradual density variations (see Electronic Supplementary Material). Importantly, these transects indicate that the strong front only persists ~1 km downstream of the tip of Jetty Island.

Frontal Persistence and Repeatability

We can combine our various measurement techniques to determine the repeatability of frontal formation over varying conditions. The boat-mounted in situ transects (both ADCP and CTD) observed the front during all large flood tides that were sampled in 2005, 2006, and 2009, although the 2006 neap tide survey (which included two large flood tides) exhibited a weaker, shorter lasting front. The AUV observed the front on the 2 days that it ran
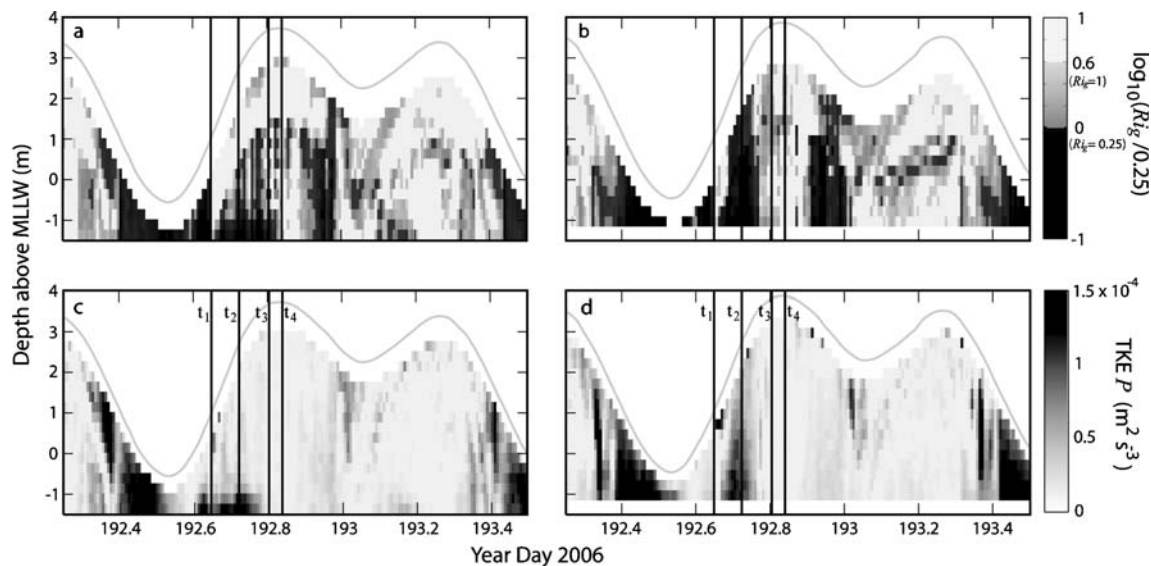
Fig. 8 Ri_g and P on either side of the front. **a**, **b** The gradient Richardson number, Ri_g, and **c**, **d** the turbulent kinetic energy production, P (m^2 s^{-3}). Ri_g is plotted on a log scale divided by its critical value, $Ri_c=0.25$. Regions of $Ri_g<0.25$ (black) have the potential to be mixed while regions with $Ri_g>1$ (light gray) are considered stable. We also call out a third region where $0.25<Ri_g<1$ (gray scale) which may include regions where mixing can still occur due to the possible case that Ri_c for this dataset is higher than 0.25 as discussed in Giddings et al. (2011). Note that Ri_g is computed using a linear interpolation of the density at the three vertically moored CTDs at each location. The left panels are measurements from mooring M3A (outer bank) while the right panels are from mooring M3B (inner bank). The time scale and time stamps marked with vertical lines are the same as those shown in Figs. 5, 6, and 9 (t_1–t_4)

transects during the strong flood tide. The TIR imagery (both near- and far-field) observed the front during all large flood tides that were sampled during the 2006 experiment (15 tides). Finally, RiverRad observed the front during all strong flood tides from peak flood to higher-high water during 2005 (18–27 July 2005) and during about half of the strong flood tides during 2007 (2–14 Aug and 27 Aug–14 Sept 2007). (These observations are summarized in the Electronic Supplementary Material.)

Our observations cover a broad range of parameter space including spring and neap tides and varying tidal asymmetry (Fig. 2). Although there were no strong trends, it appears the front is weaker during smaller tidal ranges with a relatively small following high tide. During these types of tides, the radar rarely captures the front, while the transecting instrumentation and TIR imagery captures it, but often weakly. We hypothesize this may point to a change in the frontal characteristics, rather than a disappearance of the front. Tides with a relatively low high-water and small tidal range will have a weaker momentum flux of the trapped water producing a front with distinguishable density differences but weaker convergence. Thus the radar, for which frontal detection relies on a strong velocity convergence, may not observe all weak fronts.

Examining frontal repeatability further, we combined the data that covered the full frontal progression to examine frontal longevity. This includes nine observational days, about half of which are near-field TIR and half of which are in situ measurements. A correlation between the range between lower water and higher water during the flood tide and the length of time the front persists yields a statistically significant positive correlation ($r^2=0.68$, $N=9$, $p=0.003$) confirming that larger tidal ranges lead to a longer lasting front.

Overall, we find this convergence front is a repetitive feature in this estuarine system occurring on most large flood tides (although more pronounced during stronger tides). It first appears near peak flood and persists through slack near higher-high water. The front results from a convergence of mid-density mudflat-originated water with Puget Sound density water in the main channel. The front stretches from the tip of Jetty Island to ~1 km upriver and persists for ~3 h over which time it propagates across the channel before weakening and disappearing.

Discussion

Given the recurrence of this front and its strong density and velocity signals and large influence on vertical mixing, in this section we investigate the forcing mechanisms maintaining it. The frontal evolution described in the previous section describes the bathymetric trapping mechanism for frontogenesis and frontal progression (recall Fig. 7). While the front resembles a buoyant plume front, it is not a freely propagating plume: the buoyant mudflat flow is arrested. REMUS measurements show that the interface sharpened

over time and did not progress across the channel at a constant rate nor in a consistent direction (i.e., the front occasionally moved in the opposite direction, towards the outer bank, see the Electronic Supplementary Material). To further elucidate the physical mechanisms that create, maintain, and control the front, we examine the evolution of the scalar gradient equation and the dominant forcing terms in the transverse momentum budget. We will show that this front and its propagation are maintained by strong transverse convergent circulation driven by a combination of channel curvature and lateral baroclinic forcing.

Evolution of the Lateral Salinity Gradient

To examine how fronts are created, maintained, and transformed, the derivative of the advection–diffusion equation in the cross-frontal direction can be used to understand the evolution of a scalar gradient. For the case of lateral gradients:

$$
\underbrace{\frac{\partial}{\partial t}\left(\frac{\partial C}{\partial y}\right)}_{unsteady} + \underbrace{u\frac{\partial}{\partial x}\left(\frac{\partial C}{\partial y}\right) + v\frac{\partial}{\partial y}\left(\frac{\partial C}{\partial y}\right) + w\frac{\partial}{\partial z}\left(\frac{\partial C}{\partial y}\right)}_{advection} = \underbrace{-\underbrace{\frac{\partial u}{\partial y}\frac{\partial C}{\partial x}}_{straining} - \underbrace{\frac{\partial v}{\partial y}\frac{\partial C}{\partial y}}_{convergence} - \underbrace{\frac{\partial w}{\partial y}\frac{\partial C}{\partial z}}_{stretching}}_{differential\ advection}
$$

$$
+ \underbrace{\frac{\partial}{\partial x}\left(\frac{\partial K_x}{\partial y}\frac{\partial C}{\partial x}\right) + \frac{\partial}{\partial y}\left(\frac{\partial K_y}{\partial y}\frac{\partial C}{\partial y}\right) + \frac{\partial}{\partial z}\left(\frac{\partial K_z}{\partial y}\frac{\partial C}{\partial z}\right)}_{differential\ mixing}
$$

$$
+ \underbrace{\frac{\partial}{\partial x}\left[K_x\frac{\partial}{\partial x}\left(\frac{\partial C}{\partial y}\right)\right] + \frac{\partial}{\partial y}\left[K_y\frac{\partial}{\partial y}\left(\frac{\partial C}{\partial y}\right)\right] + \frac{\partial}{\partial z}\left[K_z\frac{\partial}{\partial z}\left(\frac{\partial C}{\partial y}\right)\right]}_{diffusion\ of\ (\partial C/\partial y)} \quad (3)
$$

where C is the scalar of interest and x, y, and z denote the along-stream, cross-stream, and vertical coordinate directions, and u, v, and w are the velocity components in those respective directions. K_x, K_y, and K_z represent the along-stream, cross-stream, and vertical turbulent diffusivities for the scalar of interest. Several of these terms may work against diffusion to maintain frontal gradients. For example, intrusion (or plume) fronts are maintained by the advection of an existing gradient and convergence (terms 2–4 and 6), whereas axial convergence fronts rely on along-stream differential advection and convergence (terms 5 and 6).

Because density in this system is dominated by salinity, we consider the evolution of lateral salinity gradients. We can estimate several of these terms from our measurements: unsteadiness (term 1), lateral advection (term 3), along-stream straining (term 5), and cross-stream convergence (term 6). These terms can be estimated with the 2006 transect data near the water surface using finite differences of the near-surface salinity and velocity measurements as well as $\partial S/\partial x$ from the along-stream CTD casts. Although the results are noisy and vary somewhat depending on the choice of filtering and/or averaging, they provide order of magnitude estimates. The lateral advective and cross-stream straining terms both peak around nearly 0.01 $m^{-1}\ s^{-1}$ during the time and location where the front is present, often more than two orders of magnitude greater than the unsteady and along-stream straining terms and than any of the terms away from the frontal location. In general the lateral advective term mostly acts to enhance the lateral gradients near the front while the lateral straining term

Table 1 Magnitude of terms in the evolution of lateral salinity gradient equation near and away from the front

Term	Name	Magnitude ($m^{-1}\ s^{-1}$)	
		Near front	Away from front
$\frac{\partial}{\partial t}\left(\frac{\partial S}{\partial y}\right)$	Unsteadiness	2×10^{-4}	-9×10^{-6}
$v\frac{\partial}{\partial y}\left(\frac{\partial S}{\partial y}\right)$	Lateral advection	-9×10^{-3}	-3×10^{-5}
$\frac{\partial u}{\partial y}\frac{\partial S}{\partial x}$	Along-stream straining	1×10^{-5}	3×10^{-6}
$\frac{\partial v}{\partial y}\frac{\partial S}{\partial y}$	Cross-stream convergence	1×10^{-2}	2×10^{-5}

Terms in the evolution of lateral salinity gradient equation (Eq. 3) were calculated across the entire cross section using surface measurements. Values presented in the table include maximum values near the frontal interface (within 5 m of the maximum salinity gradient) and values far (50 m) from the frontal interface at time t_2. Note that the "near front" values are the maximum values in the vicinity of the front and thus are not all co-located. For example, at this time, the maximum straining value presented occurs at the frontal interface while the maximum lateral advective term occurs just 5 m to the side of the frontal interface. As described in the text, at this time straining dominates at the frontal interface acting to reduce frontal gradients while lateral advection dominates on either side of the interface acting to strengthen gradients

acts to decrease the lateral gradients, although there is variability depending on the exact time and cross-stream location. For example ~20 min prior to time t_2, lateral advection and straining act together to decrease the frontal strength on the trailing edge of the front, while lateral advection acts strongly to enhance the lateral gradients on the leading edge of the front. At t_2, when the front is slightly broadened but still strong, straining acts to decrease frontal gradients at the frontal interface while lateral advection dominates straining to enhance the gradients on either side of it. The magnitude of these terms at a location near and far away (50 m) from the frontal interface for time t_2 (i.e., Fig. 5d, f) are included in Table 1. Although we do not have sufficient data to calculate many of the terms, the dominance of the lateral advective and lateral convergence terms during the front seems reasonable based on the strong transverse circula-

tion associated with this front. We note that the differential vertical mixing term (term 10, Eq. 3) may play a role due to the differences in vertical mixing observed on either side of the channel (described in "Stratification and Vertical Mixing") although our data are too coarse to accurately estimate this term near the front.

Transverse Circulation and Transverse Momentum

Due to the observed strong transverse circulation and the relative importance of the lateral advective and lateral convergence terms in maintaining the front, we investigate the mechanisms driving transverse circulation. The lateral momentum equation in curvilinear coordinates (e.g., Geyer 1993; Kalkwijk and Booij 1986; Lacy and Monismith 2001) is:

$$\frac{Dv}{Dt} = \underbrace{\frac{\partial v}{\partial t}}_{acceleration} \underbrace{+ u\frac{\partial v}{\partial x} + v\frac{\partial v}{\partial y} + w\frac{\partial v}{\partial z}}_{advection} = \underbrace{\frac{u^2}{R_x}}_{\substack{centrifugal \\ (curvature)}} - \underbrace{fu}_{\substack{Coriolis \\ (rotation)}} - \underbrace{g\frac{\partial \eta}{\partial y}}_{barotropic} - \underbrace{\frac{g}{\rho_o}\left(\int_z^0 \frac{\partial \rho}{\partial y}(z')\mathrm{d}z'\right)}_{baroclinic} - \underbrace{\frac{\partial}{\partial z}(\langle v'w'\rangle)}_{friction} \tag{4}$$

where x, y, z, and u, v, w are defined above, ρ and ρ_o are the spatially varying and background density, g is gravity, $\langle v'w'\rangle$ is the cross-stream Reynolds stress, f is the Coriolis parameter ($f=1.08\times10^{-4}$ s^{-1} for our study location), η is the free surface elevation, and R_x is the radius of curvature in the streamwise direction. R_x is computed utilizing the change in the principal axes of flow direction ($\Delta\theta$) and distance between adjacent moorings (Δx) (e.g., Chant and Wilson 1997) and is positive when along-stream flow bends toward the right:

$$R_x = \frac{\Delta x}{2\sin(0.5\Delta\theta)} \tag{5}$$

With the exception of the longitudinal and vertical advective terms, we can compute the remaining terms in Eq. 4 centered near mooring M3B throughout the 2006 experiment period. These calculations well represent the dynamics driving transverse circulations that span the entire channel and in particular help identify the mechanisms driving the formation of the inner bank circulation cell. When the front is present, this bulk approximation (which includes estimates of terms using the two cross-stream moorings) becomes less relevant. Thus, we follow this bulk cross-stream momentum budget with a discussion of these terms throughout the cross section during the period of the frontal propagation.

The acceleration, centrifugal, and Coriolis terms were all estimated throughout depth using a finite difference of 10-min-averaged ADCP velocity measurements at mooring M3B. The lateral advective and pressure terms were estimated using a finite difference of velocity and pressure data between moorings M3B and M3A. The pressure data were de-trended to remove any long-term instrument drift, and the hydrostatic pressure between the instrument depths was removed. Finally, an offset was estimated assuming that when the along-stream near-bed velocity was zero, the lateral pressure gradient should be zero (Nidzieko et al. 2009). The baroclinic contribution (described below) to the total pressure gradient was removed to isolate the barotropic pressure (Geyer et al. 2000; Nidzieko et al. 2009). The baroclinic term was estimated using interpolated density profiles from the three vertical CTDs at moorings M3A and M3B. Finally, the friction (vertical divergence of stress) term was estimated using a vertical difference of the cubic spline smoothed cross-stream Reynolds stresses. Errors were estimated for all of the terms using standard error propagation analysis (e.g., Emery and Thomson 2004, Eq. 3.16.8).

In the interest of highlighting cross-stream circulation, we present a shear form of the cross-stream momentum terms in Fig. 9, near-surface values minus near-bottom values:

$$\underbrace{\frac{\partial(v_1 - v_2)}{\partial t}}_{acceleration} + \underbrace{\left(u_1 \frac{\partial v_1}{\partial x} - u_2 \frac{\partial v_2}{\partial x}\right) + \left(v_1 \frac{\partial v_1}{\partial y} - v_2 \frac{\partial v_2}{\partial y}\right) + \left(w_1 \frac{\partial v_1}{\partial z} - w_2 \frac{\partial v_2}{\partial z}\right)}_{advection}$$

$$= \underbrace{\frac{u_1^2 - u_2^2}{R_x}}_{\substack{centrifugal \\ (curvature)}} \underbrace{- f(u_1 - u_2)}_{\substack{Coriolis \\ (rotation)}} + \underbrace{\frac{g}{\rho_o}\left(\int_{z2}^{z1} \frac{\partial \rho}{\partial y}(z')\mathrm{d}z'\right)}_{baroclinic} - \underbrace{\left(\left(\frac{\partial}{\partial z}\langle v'w'\rangle\right)_1 - \left(\frac{\partial}{\partial z}\langle v'w'\rangle\right)_2\right)}_{friction} \qquad (6)$$

where 1 indicates a near-surface value and 2 indicates a near-bottom value (note: this removes the barotropic pressure gradient term). In Fig. 9, near-surface and near-bottom values are ~1 m below the surface and near the bed respectively. The friction term has large uncertainty due to the noisiness of this method in the cross-stream direction, particularly towards the water surface, thus we leave it off of Fig. 9 for clarity and incorporate it as an unknown into our residuals.

The top panel of Fig. 9 shows the cross-stream velocity shear (i.e., near-surface minus near-bottom v). Throughout much of the tidal cycle, particularly during strong along-stream currents, circulation at this mooring is in the direction expected due to the main channel curvature (i.e., towards the outer bank at the surface and towards the inner bank at depth leading to a positive velocity shear). This is consistent with a dominant balance between the sheared baroclinic pressure gradient and sheared centrifugal acceleration during the strong ebb, early strong flood, and weak ebbs (Fig. 9b) along with negligible contributions of the sheared acceleration, transverse advection, and Coriolis terms (Fig. 9c). Similarly during these times, the major balance in the depth varying momentum equation (Eq. 4, figure not shown) is between centrifugal accelerations, O (1.5×10^{-3}), and pressure (barotropic, O(1.5×10^{-3}) and baroclinic, O(1×10^{-3})). A centrifugal—pressure balance

Fig. 9 Sheared cross-stream momentum budget. **a** Cross-stream shear velocity (ms^{-1}) computed as the near-surface minus near-bottom cross-stream velocity. **b–d** Terms in the shear transverse momentum balance (Eq. 6 near surface (1) minus near bottom (2), ms$^{-2} \times 10^{-3}$) with shading indicating 95% confidence intervals. **b** The dominant terms: sheared centrifugal acceleration (*black*) and baroclinic pressure gradient (*light gray*). **c** The remaining terms (note that the *vertical scale* is the same): sheared lateral advection (*black*), Coriolis (*gray*), and unsteady (*light gray*). **d** A total residual from all of the estimated terms in (**b**) and (**c**) (*black*, effectively representing along-stream and vertical advection, friction, plus any unaccounted for errors) and from the terms remaining after a pressure-centrifugal balance (*light gray*, i. e., a residual after incorporating only the terms in (**b**), effectively representing advection, Coriolis, friction, plus any unaccounted for errors). Water level and depth averaged along-stream velocity are displayed in (**e**) and (**f**), and *vertical lines* mark the times discussed in the text
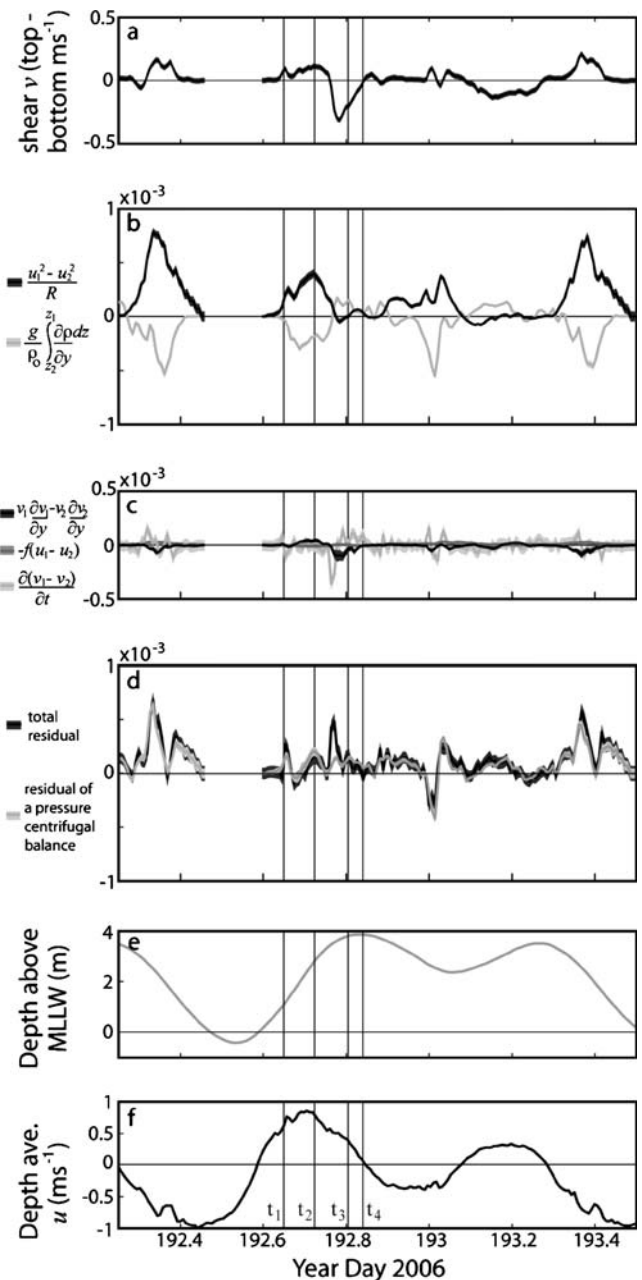
throughout the record and throughout depth (with a 3 h low-pass filter) is statistically significantly correlated ($r^2 = 0.59$, $N_{effective} = 1,513$, $p < 0.0001$), although there is still a residual (linear regression slope=0.84 ± 0.0084, intercept=$2.5 \times 10^{-5} \pm 2.2 \times 10^{-6}$). Including other terms does not reduce the residual significantly as is also evident in the shear form of the equation comparing the total shear residual to a residual just from a sheared centrifugal—pressure balance (see Fig. 9d). This indicates that throughout much of the tidal cycle, transverse circulations in this region of the SRE are driven by curvature-induced circulation modulated by lateral baroclinic gradients. Typically, as shown in Fig. 9b, cross-channel baroclinic gradients act to decrease the magnitude of the centrifugal driven secondary circulation. The nonzero (within 95% confidence intervals) shear residual (Fig. 9d) throughout much of the record indicates the additional importance of friction and potentially along-stream and/or vertical advection (similar to findings by Nidzieko et al. 2009), the latter two are often important in confluences and curved regions where helical motion exists. Finally, additional unquantified errors result from the spatial approximations.

Despite the fact that the lateral momentum budget does not close with the available data, it reveals the dominant terms throughout much of the record and provides strong evidence that the inner bank circulation cell was established via the main channel curvature, i.e., before the front passed the mooring, centrifugal acceleration and pressure dominated the balance. The bulk balance presented does begin to elucidate the frontal dynamics. When the front passed mooring M3B, (around day 192.75 between t_2 and t_3) there was a clear reversal of the transverse circulation to strong circulation reverse that expected due to curvature (Fig. 9a). The acceleration term briefly peaked during this transition (Fig. 9c). There was also a brief input of lateral advection (Fig. 9c), although this value must be underestimated due to the bulk across channel calculation. The significant decrease in magnitude of the baroclinic pressure gradient indicates that within the outer bank circulation cell the baroclinic gradients are minimal. This budget does not, however, fully describe the mechanisms driving the convergent transverse circulation associated with the front because it is based on only two points in the cross section rather than considering the full cross-sectional variability.

This analysis does not consider curvature of the mudflat flow, nor the potential for a water surface elevation that varies in the lateral direction. The main channel and the bypass region have reverse radii of curvature (see Fig. 1c, $R_x$main=860 m, $R_x$mudflats= −1,250 m computed via Eq. 5 using a mean principal axes direction from upstream moorings M3A and M3B and principal axes directions from downstream moorings M2A

and M4 for the main channel and mudflats, respectively), such that centrifugal forcing will be of opposing signs leading to a buildup of the water surface elevation mid-channel (see sketch in Fig. 7d). This can drive back-to-back surface convergent circulation similar to that observed (Fig. 5e). Similar circulation has been observed at Y-shaped junctions in rivers with negligible density effects (e.g., Ashmore et al. 1992; Rhoads and Sukhodolov 2001; Szupiany et al. 2007). The relative strength of the circulation cells in a riverine confluence is related to the ratio of the momentum flux between the two channels (Rhoads 2006). The flow through the bypass (estimated from mooring M4 and a cross-sectional area) is approximately one third of the flow through the main channel (estimated similarly using mooring M3B), therefore the fact that the outer bank circulation cell (associated with the bypass) eventually overcomes the inner bank circulation cell suggests that either there is additional unaccounted for momentum flux and/or another mechanism plays a role in the frontal progression. Additionally, the bulk balance does not account for an altered profile of centrifugal forcing which may also play a role as suggested by the along-stream velocity distributions seen in Fig. 5d.

The bulk cross-channel momentum balance showed the lateral baroclinic term was significant and we expect it must play an even more important role at the front. The bulk estimates of both the baroclinic pressure gradient and lateral advection are underestimated at the front (and overestimated away from the front) because the finite difference over the cross-section under-resolves the real gradients. We can estimate the baroclinic gradient at the front with the near-surface CTD transects as well as with the 2009 cross-stream CTD casts. For example, for the density displayed in Fig. 4a, the near-bed lateral baroclinic gradient between the two casts on either side of the front was 9×10^{-4} ms^{-2} while it was near zero between the other casts. The lateral baroclinic gradient was largest near the bed and relatively constant throughout the lower layer until reaching the base of the mudflat intrusion from where it decreased linearly to zero at the surface. Again, this is an underestimate because the distance between the two CTD casts is greater than the frontal width. Assuming that similar density gradients occur over ~10 m rather than the 60 m between casts (as suggested by the near-surface CTD measurements), the estimated lateral baroclinic gradient increases to ~5×10^{-3} ms^{-2}. Similar estimates can be made using the cross-channel moorings as well as the near-surface density assuming a layer depth. Both of these estimates also result in a lateral baroclinic gradient of ~5×10^{-3} ms^{-2} at the front and near zero elsewhere. Given an idealized buoyant plume front

(in the absence of other forcing), the baroclinic pressure gradient would be zero everywhere except over the frontal width. Initially this gradient has to be balanced by acceleration and advection (Dv/Dt). In fact, transect measurements of lateral advection across the channel (not shown) show a peak of similar magnitude but opposite sign to the baroclinic pressure gradient at the front. Because the baroclinic gradient varies with depth, it will drive a circulation cell towards the denser side near the surface and the lighter side near the bottom. This baroclinic forcing must be an important factor forming the outer bank circulation cell as well as influencing its cross-channel progression.

To further confirm the relative importance of the baroclinic and centrifugal forcing in driving the outer bank circulation cell and frontal migration, a qualitative process study was performed utilizing the validated numerical model (Wang et al. 2009; 2011; Plant et al. 2009). Starting with the same initial conditions, the strength of the baroclinic forcing was adjusted (by adjusting the saline expansivity, β) near peak flood tide just as the water over the mudflats began to flow towards the main channel. It is clear from this process study (results presented in the Electronic Supplementary Material) that density strongly influences frontal formation and migration in the model. Without density effects, the convergent transverse circulation was nearly absent and although a weak front formed, it did not move across the channel. With enhanced density effects, the front became stronger with a stronger outer bank circulation cell. These numerical process studies help support the conclusions from the data that the Y-shaped intersection alone cannot explain the front; baroclinic forcing is important in driving the outer bank circulation cell and allowing the outer bank circulation cell to eventually overcome the inner bank cell.

Therefore, based on our data, supported by the numerical study, we conclude that the outer bank circulation cell is driven by both the reversed curvature of the mudflats as well as lateral baroclinic forcing. This circulation cell does not immediately encompass the entire cross section as it is inhibited by the main channel curvature-induced circulation on the inner bank. As the flood tide weakens, centrifugal forcing decreases. In addition, the water over the mudflats are deepening and becoming denser, increasing transport into the channel from the bypass region but also limiting the source of the lateral baroclinic forcing. This is associated with the growth of the outer bank circulation cell and movement of the frontal location towards the inner bank. Ultimately, the front breaks down just before higher-high water near slack currents due to the diminishing of the mechanisms maintaining the front.

Conclusions

Our broad range of temporal and spatial observations enable us to describe in detail the evolution of a trapping-generated front, the mechanisms maintaining the front, and its influence on stratification and mixing. The front appears during most strong flood tides, although it is sharper and has stronger transverse circulation during larger tides. Mid-density water over the mudflats, trapped on the previous large ebb, converges with denser water in the main channel near peak flood. The front and associated transverse circulations and density gradients persist for ~3 h from peak currents to higher-high water during which time it progresses across the channel.

Fronts driven by bathymetric variability have been studied extensively (e.g., Nunes and Simpson 1985; Valle-Levinson et al. 2000); however, this particular trapping mechanism is not well documented. Lacy et al. (2003) provide the best description of a similar trapping mechanism in which convergence of fresher water from a shallow embayment leads to a front maintained by the interaction of lateral baroclinic forcing and bottom-generated turbulence. In the study presented here, trapping also generates lateral baroclinic forcing; however, centrifugal acceleration plays a dominant role in frontal maintenance due to the strongly curving main channel and Y-shaped junction. The strong surface convergent transverse circulation driven by curvature and lateral baroclinic forcing plays an important role in maintaining lateral gradients at the front via lateral advection and lateral convergence.

Similar to Lacy et al.'s (2003) conclusions, differential vertical mixing in this system may additionally play a role in hindering frontal progression; however, it is difficult to tease out as the front itself influences vertical mixing and our mixing measurements are coarse. The northern side of the front exhibits increased stratification and decreased vertical mixing. Importantly, after the front has progressed across the channel and ultimately disappeared, vertical stratification and reduced mixing across the channel are maintained at the end of the large flood, reverse that expected in estuarine systems due to SIPS. Enhanced stratification at the end of flood tides has been observed due to lateral flows in other systems (e.g., Scully et al. 2009).

As described in the "Introduction," fronts have been shown to influence the transport of a variety of water-borne constituents including phytoplankton, larvae, sediment, and pollutants. The front and associated transverse circulation and altered vertical mixing likely influence important shoal/channel transport pathways in the SRE. The Snohomish basin is one of the primary producers of anadromous salmonids in Puget Sound (Haring 2002) and also provides important habitat for Dungeness crabs. For these species, intertidal and shallow subtidal areas and

marsh regions are important for rearing juveniles and in the early stages of their life, dispersal by currents are important. In fact, hydrodynamic simulations conducted by Yang and Khangaonkar (2005) and Yang et al. (2010) aimed to address proposed marsh restoration efforts in the SRE suggest that the mudflat regions are important for transport and trapping of sediment and juvenile fish. Thus, the hydrodynamic connectivity between the mudflats and main channel, which is mitigated by the frontal presence plays in important role in these transport processes.

Although this particular geometry is a bit unusual, similar geometry is expected in braided rivers and deltas such as in the Columbia River (Jay and Smith 1990) where channels across intertidal flats may transport momentum and salt. Despite, the odd bathymetry, this front fits within the broader context of bathymetrically generated fronts. The generating mechanism is similar to differential advection in that there is a phasing difference between the mudflats and the main channel and the geometry shares similarities to separation fronts. As a result, we hypothesize that trapping fronts of this type are common amongst other estuarine systems with broad shoals, intertidal regions, sub-embayments, or braided channels and will consequently have similar effects on stratification, vertical mixing, and transport processes in other systems.

References

Ashmore, P.E., R.I. Ferguson, K.L. Prestegaard, P.J. Ashworth, and C. Paola. 1992. Secondary flow in anabranch confluences of a braided, gravel-bed stream. *Earth Surface Processes and Landforms* 17: 299–311. doi:10.1002/esp.3290170308.

Braun, N., F. Ziemer, A. Bezuglov, M. Cysewski, and G. Schymura. 2008. Sea-surface current features observed by Doppler radar. *IEEE Transactions on Geoscience and Remote Sensing* 46: 1125–1133.

Brown, J., W.R. Turrell, and J.H. Simpson. 1991. Aerial surveys of axial convergent fronts in the UK estuaries and the implications for pollution. *Marine Pollution Bulletin* 22: 397–400.

Chant, R.J. 2002. Secondary circulation in a region of flow curvature: relationship with tidal forcing and river discharge. *Journal of Geophysical Research* 107: 3131–3141.

Chant, R.J., and R.E. Wilson. 1997. Secondary circulation in a highly stratified estuary. *Journal of Geophysical Research* 102: 23207–23215.

Chickadel, C.C., A.R. Horner-Devine, S.A. Talke, and A.T. Jessup. 2009. Vertical boil propagation from a submerged estuarine sill. *Geophysical Research Letters* 36: L10601. doi:10.1029/2009GL037278.

Dronkers, J., and J.T.F. Zimmerman. 1982. Some principles of mixing in tidal lagoons. Oceanologica acta. Proceedings of the International Symposium on Coastal Lagoons, Bordeaux, France, 9–14 September, 1981. pp. 107–117.

Duck, R.W., and S.F.K. Wewetzer. 2001. Impact of frontal systems on estuarine sediment and pollutant dynamics. *The Science of the Total Environment* 266: 23–31.

Emery, W.J., and R.E. Thomson. 2004. *Data analysis methods in physical oceanography*, 2nd ed. Amsterdam: Elsevier.

Falcon, M. 1984. Secondary flow in curved open channels. *Annual Review of Fluid Mechanics* 16: 179–193.

Farmer, D.M., E.A. D'asaro, M.V. Trevorrow, and G.T. Dairiki. 1995. Three-dimensional structure in a tidal convergence front. *Continental Shelf Research* 15: 1649–1673.

Farmer, D., R. Pawlowicz, and R. Jiang. 2002. Tilting separation flows: a mechanism for intense vertical mixing in the coastal ocean. *Dynamics of Atmospheres and Oceans* 36: 43–58. doi:10.1016/S0377-0265(02)00024-6.

Fischer, H.B. 1972. Mass transport mechanisms in partially stratified estuaries. *Journal of Fluid Mechanics* 53: 671–687.

Fischer, H.B., E.J. List, R.C.Y. Koh, J. Imberger, and N.H. Brooks. 1979. *Mixing in inland and coastal waters*. San Diego: Academic.

Franks, P.J.S. 1992. Phytoplankton blooms at fronts: patterns, scales, and physical forcing mechanisms. *Reviews in Aquatic Sciences* 6: 121–137.

Fringer, O.B., M. Gerritsen, and R.L. Street. 2006. An unstructured-grid, finite-volume, nonhydrostatic, parallel coastal ocean simulator. *Ocean Modelling* 14: 139–173. doi:10.1016/j.ocemod.2006.03.006.

Gargett, A.E., and J.N. Moum. 1995. Mixing efficiencies in turbulent tidal fronts: results from direct and indirect measurements of density flux. *Journal of Physical Oceanography* 25: 2583–2608.

Geyer, W.R. 1993. Three-dimensional tidal flow around headlands. *Journal of Geophysical Research* 98: 955–966.

Geyer, W.R., J.H. Trowbridge, and M.M. Bowen. 2000. The dynamics of a partially mixed estuary. *Journal of Physical Oceanography* 30: 11629–11637.

Giddings, S.N., D.A. Fong, and S.G. Monismith. 2011. The role of straining and advection in the intratidal evolution of stratification, vertical mixing, and longitudinal dispersion of a shallow, macrotidal, salt-wedge estuary. *Journal of Geophysical Research* 116: C03003. doi:10.1029/2010JC006482.

Handler, R.A., R.P. Mied, T.E. Evans, and T.F. Donato. 2001. Convergence fronts in tidally forced rotating estuaries. *Journal of Geophysical Research* 106: 27145–27162. doi:10.1029/2000JC000637.

Haring, D. 2002. Salmonid habitat limiting factors analysis, final report. Olympia: Washington State Conservation Commission.

Huzzey, L.M., and J.M. Brubaker. 1988. The formation of longitudinal fronts in a coastal plain estuary. *Journal of Geophysical Research* 93: 1329–1334. doi:10.1029/JC093iC02p01329.

Jay, D.A., and J.D. Smith. 1990. Residual circulation in shallow estuaries. 1. Highly stratified, narrow estuaries. *Journal of Geophysical Research* 95: 711–731. doi:10.1029/JC095iC01p00711.

Kalkwijk, J.P.T., and R. Booij. 1986. Adaptation of secondary flow in nearly-horizontal flow. *Journal of Hydraulic Research* 24: 19–37.

Klemas, V., and D.F. Polis. 1977. A study of density fronts and their effects on coastal pollutants. *Remote Sensing of Environment* 6: 95–126.

Lacy, J.R., and S.G. Monismith. 2001. Secondary currents in a curved, stratified, estuarine channel. *Journal of Geophysical Research* 106: 31283–31302.

Lacy, J.R., M.T. Stacey, J.R. Burau, and S.G. Monismith. 2003. Interaction of lateral baroclinic forcing and turbulence in an estuary. *Journal of Geophysical Research* 108: 3089–3103. doi:10.1029/2002JC001392.

Largier, J.L. 1993. Estuarine fronts: how important are they? *Estuaries* 16: 1–11.

Le Fevre, J. 1986. Aspects of the biology of frontal systems. *Advances in Marine Biology* 23: 163–299.

Li, C., and J. O'Donnell. 1997. Tidally driven residual circulation in shallow estuaries with lateral depth variation. *Journal of Geophysical Research* 102: 27915–27929.

Lu, Y., and R.G. Lueck. 1999. Using a broadband ADCP in a tidal channel. Part II: Turbulence. *Journal of Atmospheric and Oceanic Technology* 16: 1568–1579.

MacDonald, D.G., and W.R. Geyer. 2004. Turbulent energy production and entrainment at a highly stratified estuarine front. *Journal of Geophysical Research* 109: C05004.

MacVean, L.J., and M.T. Stacey. 2010. Estuarine dispersion from tidal trapping: a new analytical framework. *Estuaries and Coasts* 1–15. doi:10.1007/s12237-010-9298-x.

Nidzieko, N.J., D.A. Fong, and J.L. Hench. 2006. Comparison of Reynolds stress estimates derived from standard and fast-ping ADCPs. *Journal of Atmospheric and Oceanic Technology* 23: 854–861.

Nidzieko, N.J., J.L. Hench, and S.G. Monismith. 2009. Lateral circulation in well-mixed and stratified estuarine flows with curvature. *Journal of Physical Oceanography* 39: 831–851.

Nunes, R.A., and J.H. Simpson. 1985. Axial convergence in a well-mixed estuary. *Estuarine, Coastal and Shelf Science* 20: 637–649. doi:10.1016/0272-7714(85)90112-X.

O'Donnell, J. 1993. Surface fronts in estuaries: a review. *Estuaries* 16: 12–39.

O'Donnell, J., S.G. Ackleson, and E.R. Levine. 2008. On the spatial scales of a river plume. *Journal of Geophysical Research* 113: C04017. doi:10.1029/2007JC004440.

Okubo, A. 1973. Effect of shoreline irregularities on streamwise dispersion in estuaries and other embayments. *Journal of Sea Research* 6: 213–224.

Plant, W.J., W.C. Keller, and K. Hayes. 2005. Measurement of river surface currents with coherent microwave systems. *IEEE Transactions on Geoscience and Remote Sensing* 43: 1242–1257.

Plant, W.J., R. Branch, G. Chatham, C.C. Chickadel, K. Hayes, B. Hayworth, A.R. Horner-Devine, A.T. Jessup, D.A. Fong, O.B. Fringer, S.N. Giddings, S.G. Monismith, and B. Wang. 2009. Remotely sensed river surface features compared with modeling and in situ measurements. *Journal of Geophysical Research* 114: C11002. doi:10.1029/2009JC005440.

Rhoads, B.L. 2006. Scaling of confluence dynamics in river systems: some general considerations. In *River, coastal and estuarine morphodynamics*, ed. G. Parker and M.H. Garcia, 379–387. London: Taylor & Francis.

Rhoads, B.L., and A.N. Sukhodolov. 2001. Field investigation of three-dimensional flow structure at stream confluences: 1. Thermal mixing and time-averaged velocities. *Water Resources Research* 37: 2393–2410. doi:10.1029/2001WR000316.

Scully, M.E., and C.T. Friedrichs. 2007. The importance of tidal and lateral asymmetries in stratification to residual circulation in partially mixed estuaries. *Journal of Physical Oceanography* 37: 1496–1511.

Scully, M.E., W.R. Geyer, and J.A. Lerczak. 2009. The influence of lateral advection on the residual estuarine circulation: a numerical modeling study of the Hudson River estuary. *Journal of Physical Oceanography* 39: 107.

Sharples, J., and J.H. Simpson. 1993. Periodic frontogenesis in a region of freshwater influence. *Estuaries* 16: 74–82.

Simpson, J.H., and J.R. Hunter. 1974. Fronts in the Irish Sea. *Nature* 250: 404–406. doi:10.1038/250404a0.

Simpson, J.H., and W.R. Turrell. 1986. Convergent fronts in the circulation of tidal estuaries. In *Estuarine variability*, ed. D.A. Wolfe, 139–152. New York: Academic Press.

Simpson, J.H., J. Brown, J. Matthews, and G. Allen. 1990. Tidal straining, density currents, and stirring in the control of estuarine stratification. *Estuaries* 13: 125–132.

Smith, R. 1976. Longitudinal dispersion of a buoyant contaminant in a shallow channel. *Journal of Fluid Mechanics* 78: 677–688.

Smith, R. 1980. Buoyancy effects upon longitudinal dispersion in wide well-mixed estuaries. *Philosophical Transactions of the Royal Society of London, Series A, Mathematical and Physical Sciences* 296: 467–496.

Smith, R. 1996. Combined effects of buoyancy and tides upon longitudinal dispersion. *Coastal and Estuarine Studies* 53: 319–329.

Stacey, M.T., S.G. Monismith, and J.R. Burau. 1999. Measurements of Reynolds stress profiles in unstratified tidal flow. *Journal of Geophysical Research* 104: 10933–10949. doi:10.1029/1998JC900095.

Szupiany, R.N., M.L. Amsler, J.L. Best, and D.R. Parsons. 2007. Comparison of fixed- and moving-vessel flow measurements with an aDp in a large river. *Journal of Hydraulic Engineering* 133: 1299–1309. doi:10.1061/(ASCE)0733-9429(2007)133:12(1299.

Turner, J.S. 2001. The stability of a free shear layer. In *in Fluids*, reprintth ed, ed. B. Effects, 92–107. Cambridge: Cambridge University Press.

Valle-Levinson, A., and K.M.M. Lwiza. 1995. The effects of channels and shoals on exchange between the Chesapeake Bay and the adjacent ocean. *Journal of Geophysical Research* 100: 18551–18563.

Valle-Levinson, A., C. Li, K. Wong, and K.M.M. Lwiza. 2000. Convergence of lateral flow along a coastal plain estuary. *Journal of Geophysical Research* 105: 17045–17061. doi:10.1029/2000JC900025.

Wang, B., O.B. Fringer, S.N. Giddings, and D.A. Fong. 2009. High-resolution simulations of a macrotidal estuary using SUNTANS. *Ocean Modelling* 26: 60–85. doi:10.1016/j.ocemod.2008.08.006.

Wang, B., S.N. Giddings, O.B. Fringer, E.S. Gross, D.A. Fong, and S.G. Monismith. 2011. Modeling and understanding turbulent mixing in a macrotidal salt wedge estuary. *Journal of Geophysical Research* 116: C02036. doi:10.1029/2010JC006135.

Wolanski, E., and W.M. Hamner. 1988. Topographically controlled fronts in the ocean and their biological influence. *Science* 241: 177–181.

Yang, Z., and T. Khangaonkar. 2005. Modeling of salt intrusion, intertidal mixing, and circulation in a braided estuary. *Journal Coastal Research* 52: 171–180. doi:10.2112/1551-5036-52.sp1.171.

Yang, Z., T. Khangaonkar, M. Calvi, and K. Nelson. 2010. Simulation of cumulative effects of nearshore restoration projects on estuarine hydrodynamics. *Ecological Modelling* 221: 969–977. doi:10.1016/j.ecolmodel.2008.12.006.

Yoder, J.A., S.G. Ackleson, R.T. Barber, P. Flament, and W.M. Balch. 1994. A line in the sea. *Nature* 371: 689–692.